JACS
JOURNAL OF THE AMERICAN CHEMICAL SOCIETY
pubs.acs.org/JACS
Article

Synchronous Redox Reactions in Copper Oxalate Enable High-Capacity Anode for Proton Battery

Wanxin Song, Jianyong Zhang, Cheng Wen, Haiyan Lu, Chunhua Han, Lin Xu,* and Liqiang Mai*

Cite This: J. Am. Chem. Soc. 2024, 146, 4762−4770
Read Online

ABSTRACT: Proton batteries are competitive due to their merits such as high safety, low cost, and fast kinetics. However, it is generally difficult for current studies of proton batteries to combine high capacity and high stability, while the research on proton storage mechanism and redox behavior is still in its infancy. Herein, the polyanionic layered copper oxalate is proposed as the anode for a high-capacity proton battery for the first time. The copper oxalate allows for reversible proton insertion/extraction through the layered space but also achieves high capacity through synchronous redox reactions of Cu^{2+} and $C_2O_4^{2-}$. During the discharge process, the bivalent Cu-ion is reduced, whereas the C═O of the oxalate group is partially converted to C−O. This synchronous behavior presents two units of charge transfer, enabling the embedding of two units of protons in the (110) crystal face. As a result, the copper oxalate anode demonstrates a high specific capacity of 226 mAh g^{-1} and maintains stable operation over 1000 cycles with a retention of 98%. This work offers new insights into the development of dual-redox electrode materials for high-capacity proton batteries.

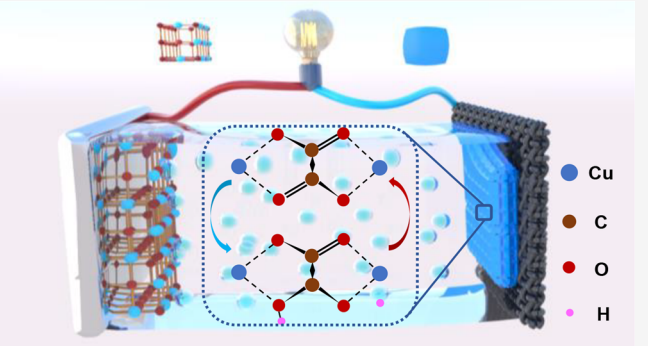

INTRODUCTION

Rechargeable batteries are regarded as an effective solution for the energy crisis, and aqueous batteries have been widely concerned because of their characteristic advantages such as high safety, low cost, high ionic conductivity, and environmental friendliness.[1−4] Usually, the charge carriers in aqueous batteries are limited to Zn^{2+} or alkali metal ions such as Li^+, Na^+, and K^+.[5−8] However, the metal ions often exist as the form of hydrates with enormous ionic radii in the electrolyte, further resulting in lower diffusion kinetics.[9,10] In contrast, the unique Grotthuss mechanism of protons can overcome the problem of slow kinetics caused by solvation, allowing for fast protons transportation through the hydrogen bond network.[11−13] Along with the advantages of abundant availability and minimum ionic radius, protons have lately been explored as potential carriers for new aqueous batteries.[14−17]

Currently, Prussian blue analogues (PBA), transition metal oxides, and other materials with three-dimensional space have been probed for proton energy storage.[3,18−21] Ji and co-workers introduced a PBA material of $Cu[Fe\text{-}(CN)_6]_{0.63}\cdot\square_{0.37}\cdot 3.4H_2O$, which utilizes the Grotthuss proton conduction mechanism to achieve an excellent rate performance of 4000 C with 50% of its 1 C capacity.[22] Xia and co-workers employed the polyanionic material VPO_4F to serve as a high-voltage proton cathode, which delivers a specific capacity of 116 mAh g^{-1} at 1 V (vs SHE).[23] Ji and co-workers used $WO_3\cdot 0.6H_2O$ with a channel structure as an anode material for proton battery, exhibiting a specific capacity of 90 mAh g^{-1} at 2 A g^{-1} and an extremely long life of 20,000 cycles.[24] However, all of the above electrode materials rely only on the redox reactions of transition metal ions to transfer charge, resulting in unsatisfactory capacities. Thus, developing high-capacity proton host electrode materials remains a significant challenge in aqueous proton batteries for large-scale energy storage applications.

Herein, for the first time, we employed polyanionic layered copper oxalate (CuC_2O_4) as a high-capacity anode material for proton batteries. In addition, we revealed the synchronous redox reactions of Cu^{2+} and the oxalate group ($C_2O_4^{2-}$) in intercalation chemistry. During charge and discharge, both the Cu-ion and C═O functional group in copper oxalate act as the redox centers, which includes the reversible transformation of Cu^{2+}/Cu^+ and C═O/C−O, accompanied by the coordination reaction of H^+. Moreover, the vertical lamellar structure of copper oxalate along the (110) crystal plane provides an embedding environment for protons. In situ XRD manifests the proton insertion/extraction behavior inside. It is demonstrated that the CuC_2O_4 electrode can withstand static

Received: November 13, 2023
Revised: January 25, 2024
Accepted: January 25, 2024
Published: February 7, 2024

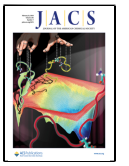

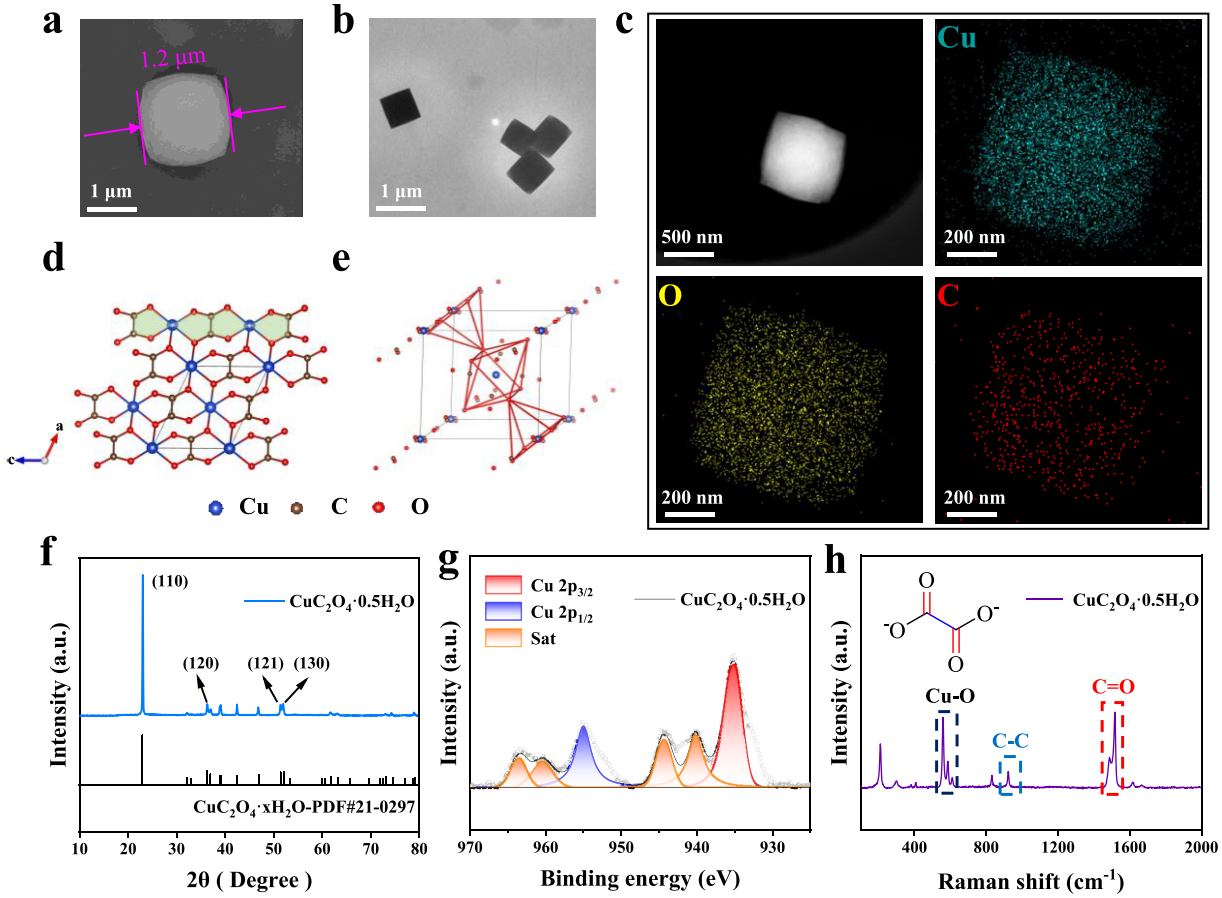

Figure 1. Morphology and structure characterization of cubic-like $CuC_2O_4{\cdot}0.5H_2O$ ($CuCO_x$ for short). (a) SEM image, (b) TEM image, (c) HAADF-STEM image, and element maps. (d) Projection along the (010) direction of the model structure of $CuCO_x$. (e) Full octahedron and two half Cu−O octahedra of one unit cell. (f) XRD pattern, (g) Cu 2p XPS spectrum, and (h) Raman spectrum of $CuCO_x$ powder.

cycling up to 1000 times while delivering a high specific capacity of 226 mAh g^{-1} with a retention of 98%. Overall, our work not only delineates the unique mechanism of proton storage in copper oxalate but also offers a possibility for the development of new dual-redox electrode materials for high-capacity proton batteries.

RESULTS AND DISCUSSION

$CuC_2O_4{\cdot}0.5H_2O$ ($CuCO_x$ for short) with a steady cubic morphology was quickly obtained by using a simple one-step synthesis method in an aqueous solvent at 30 °C (Figure S1). The spontaneous self-assembly of cubic $CuCO_x$ was found to be relatively rapid through TEM analysis of different time gradients (Figure S2). Under entirely aqueous solvent conditions, $CuCO_x$ crystals nucleated promptly, followed by the rapid growth of four hydrophilic ε-surfaces.[25] Consequently, micrometer-sized supracrystals were obtained within just 1 min. It is important to note that this growth process differs significantly from that observed in other mixed organic solvents.[26−28] Over time, the cubic edges tended to round due to the radial extension of the ε-surfaces. After an aging period of 2 weeks, the surface of $CuCO_x$ supracrystals appeared rough, indicating a trace of reverse dissolution caused by decreased ion concentration in the solvent. Although $CuCO_x$ nucleated swiftly, a short stirring time caused poor crystallinity. In experiments, a synthesis time of 30 min was determined to be the most appropriate. SEM and TEM analysis showed that $CuCO_x$ exhibited a satisfactory cubic morphology with a size of approximately one micrometer and relatively flat surfaces (Figure 1a,b). Elemental maps demonstrated an even distribution of all elements within $CuCO_x$ (Figure 1c). The refined crystallographic structure depicted in Figure 1d illustrates the projection model of $CuCO_x$ along the (010) direction in the $P12_1/n1$ setting. The green part represents the layered stacking unit of $CuCO_x$, with layers connected by Cu−O bonds. The gray box in Figure 1e indicates a cell structure in which the Cu atom is located in the center of the body and an octahedron consisting of six O atoms.[29] Notably, the stacking faults occurring frequently in the layered structure are ignored in this model to facilitate the comprehension of the system. In the XRD pattern, all diffraction peaks are well indexed to the monoclinic phase $CuCO_x$, and the (110) facets dominate the structure, which confirms the layered structure of $CuCO_x$ (Figure 1f). By selected area electron diffraction (SAED), it is found that although $CuCO_x$ has excellent crystallization, it will rapidly suffer amorphous transformation under the bombardment of high-energy electron beams; therefore, observation of diffraction patterns and lattice fringe information failed (Figure S3). The standard PDF card indicates that the crystal water content of $CuCO_x$ is x ($0 < x < 1$). This uncertainty indicates that the water inside does not participate in the crystal structure but is only isolated in the lattice, which is also indicated by the refined crystallographic structure. Thermogravimetry analyses (TGA) revealed the presence of $0.5H_2O$ per $CuCO_x$ formula unit (Figure S4). Based on the TGA data, it was discovered that $CuCO_x$ exhibits a disadvantageous high-

https://doi.org/10.1021/jacs.3c12710
J. Am. Chem. Soc. 2024, 146, 4762−4770

temperature resistance common to other oxalate materials.[27,30−32] Therefore, copper oxalate was not dehydrated. At the same time, as water in the copper oxalate does not participate in the lattice formation, the electrode performance will not be significantly affected if it remains within the material. In the XPS spectrum, the binding energies at 935.9 and 955.8 eV correspond to $2p_{3/2}$ and $2p_{1/2}$ of Cu^{2+}, respectively, while the other peaks belong to the particular satellite peaks of bivalent copper (Figure 1g). The XPS survey spectra of C and O are represented in Figure S5, which is well consistent with the reported data.[26,33−36] With the analysis of Cu 2p core excitation, it has been proven that the copper ions in the synthesized $CuCO_x$ are all in the bivalent state with no impurities present. The conclusion is further confirmed by Raman spectra, where the characteristic peaks at 560, 922, and 1516 cm^{-1} are severally derived from the vibrations of Cu−O, C−C, and C═O, respectively (Figure 1h).[37−39]

To determine the proton storage capability of the $CuCO_x$ electrode, electrochemical measurements were performed using a three-electrode system, which could provide a more stable potential for the overall system and ensure greater accuracy in determining the reaction potential of the working electrode. Furthermore, by assessing different electrolytes (Figure S6), H_2SO_4 was selected as the most suitable electrolyte because of the high activity of the electrode inside. To create a relatively mild operating environment for the $CuCO_x$ electrode, we compared the electrochemical performance of 0.1 M H_2SO_4 to the commonly used 1 M H_2SO_4, since oxalates are not resistant to acid corrosion. As evidenced in Figure S7a, a decrease in salt concentration leads to a reduction in conductivity of 0.1 M H_2SO_4, manifested as a resistance of 1.3 ohms, while 1 M is 0.3 ohms. The electrochemical stability of 1 M H_2SO_4 and 0.1 M H_2SO_4 electrolyte was evaluated by linear scan voltammetry (LSV), which indicates that the reduction of acid concentration did not cause a narrowing of the electrochemical window (Figure S7b). In addition, as shown in Figure S8, $CuCO_x$ exhibited a more stable voltage and similar capacity in the 0.1 M H_2SO_4 electrolyte compared to other higher concentrations of H_2SO_4. Based on the above data, 0.1 M H_2SO_4 was determined as the electrolyte for subsequent battery tests. In particular, the Swagelok three-electrode mold used in the experimental setup differs from the traditional electrolytic cell form, and the details are displayed in Figure S9.

As shown in Figure 2a, the cyclic voltammetry (CV) test at various scan rates from 0.1 to 0.5 mV s^{-1} was performed on the $CuCO_x$ electrode to evaluate the redox potential. The CV curves displayed a pair of pronounced redox peaks at −0.35/−0.45 V. Judging from the shape of CV curves, the pseudocapacitance effect on the surface of the carbon cloth collector influences the test. Therefore, CV measurements were conducted on $CuCO_x$ loaded on titanium foil to assess this influence, and it was found that the oxidation/reduction reaction potential was identical (Figure S10). The CV curves of $CuCO_x$ for the initial three cycles revealed an irreversible side effect occurring at a lower potential in the first cycle. According to the equation $i = av^b$, a and b are parameters, i is the peak current, and v is the scanning rate. The b values of the $CuCO_x$ electrode are 0.41 and 0.52, indicating that ionic diffusion dominates the electrochemical process rather than capacitive behavior.[22,40−42] Comparing the electrochemical impedance of $CuCO_x$ on the titanium foil and the carbon cloth collector (Figure S11) revealed that the carbon cloth had

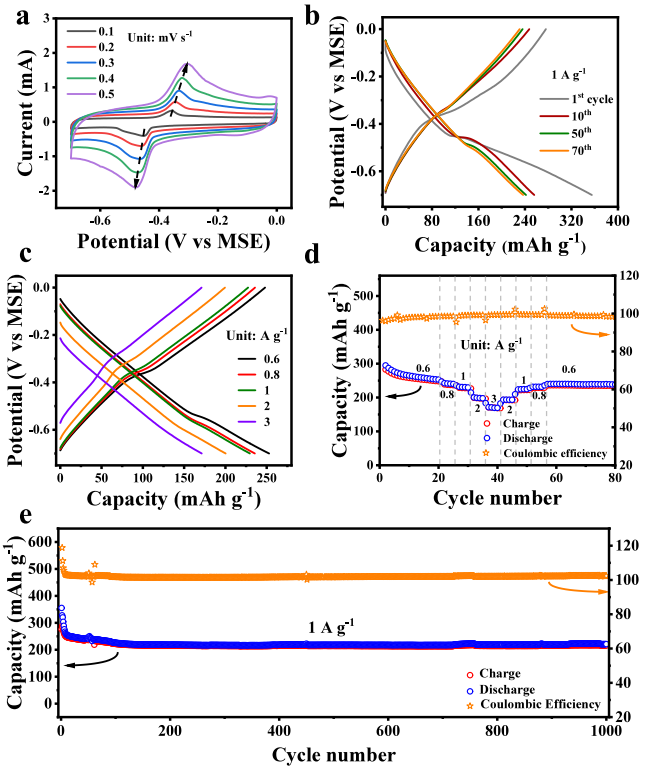

Figure 2. Electrochemical performance of the $CuCO_x$ half-cell in a typical three-electrode system. (a) CV curves of $CuCO_x$ electrode at various scan rates. (b) GCD voltage profiles of different cycles at 1 A g^{-1}. (c) GCD curves and (d) rate capability at different current densities. (e) Cycling performance at 1 A g^{-1}.

higher resistance due to poor contact. To further explore the electrochemical effect of the carbon cloth collector on the test, a separate measurement was performed (Figure S12). It can be observed in the CV curve that there is a pseudocapacitance reaction at the potential of −0.65 V, which explains why the CV curves of the $CuCO_x$ electrode failed to return to the baseline after discharge. Additionally, it should be mentioned that carbon cloth contributes only a fraction of capacity. Figure 2b shows the galvanostatic charge/discharge (GCD) voltage profiles at a current density of 1 A g^{-1}, which is very consistent with the CV curves. The initial several cycles exhibited significant excess discharge due to partially irreversible protons insertion. Afterward, excess discharge continued until the 10th cycle, followed by a slight decrease in capacity during the subsequent 60 cycles, which is on the count of unfirm bonding of $CuCO_x$ active particles on the carbon cloth collector, resulting in a small amount of stripping. Figure 2c,d demonstrates that the specific capacity of the $CuCO_x$ electrode slightly decreased with the increase of current density, while the voltage remained stable. Even at a current density of 3 A g^{-1}, the $CuCO_x$ electrode still delivers a reversible capacity of 170 mAh g^{-1}, showcasing excellent electrochemical reaction kinetics. The cyclic performance of $CuCO_x$ was investigated at a current density of 1 A g^{-1}. It is noted that after 70 cycles of active particle stripping, the reversible capacity of the $CuCO_x$ electrode remained stable at 226 mAh g^{-1}, maintaining approximately 98% (220.8 mAh g^{-1}) of the initial capacity after 1000 cycles, which demonstrates commendable cycling stability of the $CuCO_x$ electrode (Figure 2e). In addition, the

https://doi.org/10.1021/jacs.3c12710
J. Am. Chem. Soc. 2024, 146, 4762−4770

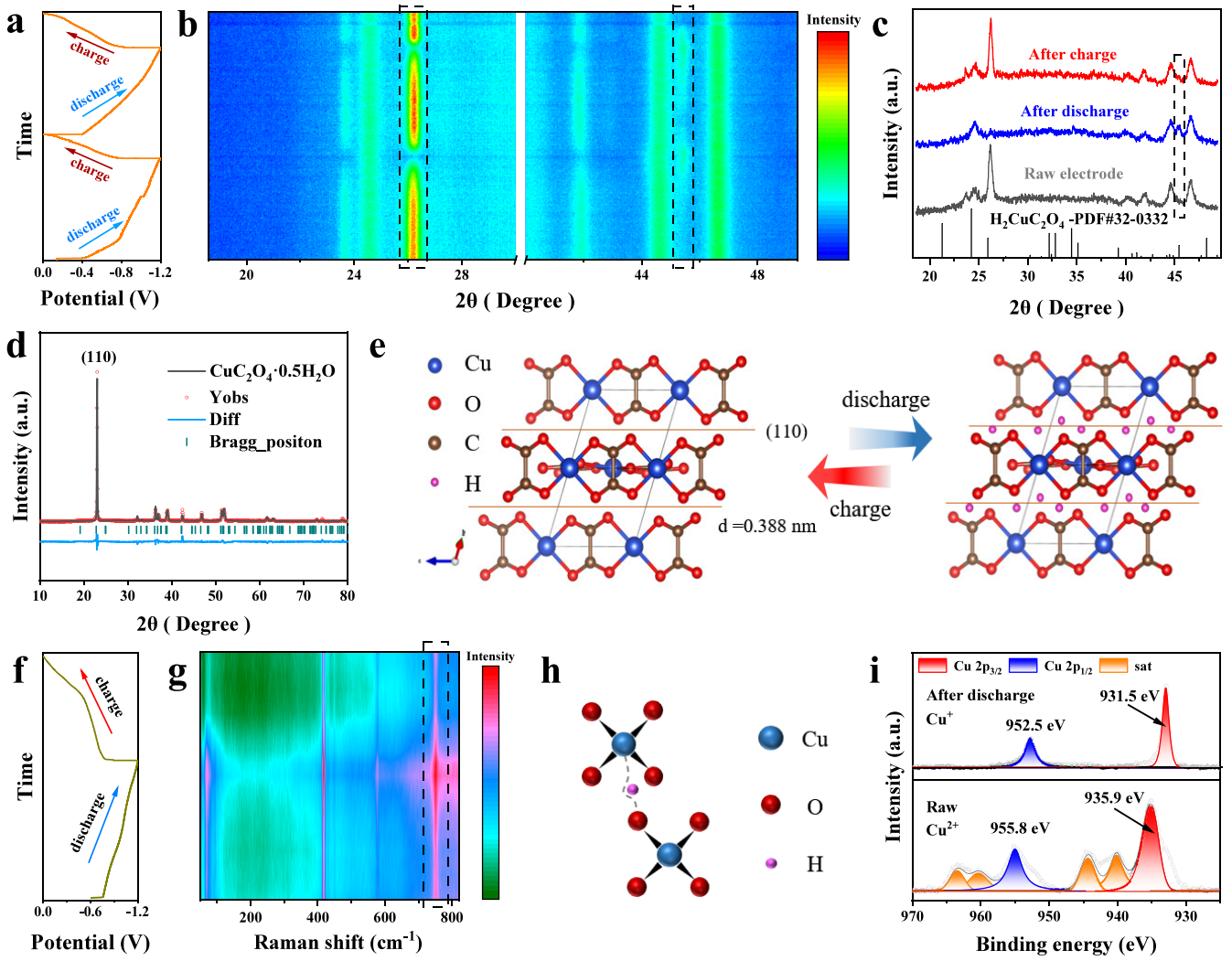

Figure 3. Proton intercalation mechanism of the $CuCO_x$ electrode. (b) In situ XRD (Co Kα) pattern of $CuCO_x$ for two full cycles as displayed in (a). The characteristic peaks are highlighted inside. (c) XRD spectra of $CuCO_x$ in different states. The standard PDF card of $H_2CuC_2O_4$ is displayed downward. (d) Rietveld refinement of powder XRD (Cu Kα) on the standard sample. (e) Schematic illustration of the proton storage process in charge/discharge states. (g) In situ Raman patterns of $CuCO_x$ electrode in the window of −1.2 to 0 V as displayed in (f). (h) Model illustration of the C−O bond flexural vibration caused by proton embedding. (i) Ex situ XPS spectra of the $CuCO_x$ electrode.

half-cell showed less self-discharge phenomenon after resting for 30 h (Figure S13).

The structure evolution of $CuCO_x$ during charge and discharge was analyzed by in situ XRD. Due to the limitation of the device, the test was conducted using a two-electrode system. The CV curve of the window from −1.2 to 0 V for the $CuCO_x$ electrode in a two-electrode cell is presented in Figure S14. In addition, it should be noted that the target used in the in situ XRD equipment was Co (Kα, 1.78886 Å) rather than Cu target (Kα, 1.5406 Å) for powder measurement. As demonstrated in Figure S15, the XRD peak positions obtained from the Co target shifted to a higher degree than those of the Cu target. From the in situ XRD pattern shown in Figure 3b, an apparent phase transformation occurred periodically during two complete discharge−charge cycles (Figure 3a). Upon discharging to −1.2 V, the diffraction peak of (110) at 26.1° vanished, along with the appearance of a new peak at 45.3°, which corresponds to the PDF standard card of $H_2CuC_2O_4$ (CuC_2O_4 combined with two H^+), indicating that the crystal structure of $CuCO_x$ underwent a change with the insertion of two units of protons (Figure 3c). Further, when the cell was recharged to 0 V, the XRD pattern was restored to its original position, thereby proving the reversibility of the proton intercalation reaction in the $CuCO_x$ electrode. The Rietveld refinement results for $CuCO_x$ powder are displayed in Figure 3d, with the differences attributed to stacking faults and trace lattice defects.[29,43−45] The proton insertion/extraction process in the $CuCO_x$ electrode is schematically illustrated in Figure 3e. During discharging, two-unit protons are inserted in (110) layers (d = 0.388 nm), transforming $CuCO_x$ into $H_2CuC_2O_4$. In subsequent charging, the protons were extracted, returning the $CuCO_x$ electrode to its original state. In situ Raman analysis of the $CuCO_x$ electrode was performed at low wavenumbers to verify the proton intercalation process further, as higher wavenumbers tend to exhibit severe fluorescence effects (Figure S16). From the in situ Raman pattern (Figure 3f,g), the peak at approximately 750 cm^{-1} showed periodic fluctuation during the cycle, corresponding to the bending vibration of the C−O bond, confirming that protons were embedded in the layers connected by the C−O bond (Figure 3h).[37,46] Thus, it further demonstrates the reversible intercalating chemistry of protons in the $CuCO_x$ electrode.

https://doi.org/10.1021/jacs.3c12710
J. Am. Chem. Soc. 2024, 146, 4762−4770

The redox mechanism of copper was analyzed by XPS spectroscopy. For clarity, only the XPS spectra at the original/discharged states of the $CuCO_x$ electrode were presented. As displayed in Figure 3i, in the initial state, the peaks at 935.9 and 955.8 eV correspond to $2p_{3/2}$ and $2p_{1/2}$ of Cu^{2+}, respectively. After being fully discharged, only Cu^{+} peaks (931.5 and 952.5 eV) were observed, and the characteristic satellite peaks of Cu^{2+} disappeared, indicating a complete redox reaction.[33,34]

It is worth noting that $CuCO_x$ exhibited a maximum capacity of 350 mAh g^{-1}, equivalent to a CuC_2O_4 molecule combining two protons, which is consistent with the results of in situ XRD. However, this would lead to an incomprehensible charge balance. Theoretically, the conversion of Cu^{2+} to Cu^{+} transfers only one electron, combining one proton, which contradicts the above conclusion and fails to achieve the capacity observed in this work. In fact, the charge compensation brought by the redox reaction of the oxalate ($C_2O_4^{2-}$) group is responsible for this.[38]

To investigate the redox behavior of the oxalate group, in situ FTIR and ex situ Raman spectra of high wavenumbers were analyzed. The FTIR spectra of $CuCO_x$ raw materials are shown in Figure S17. The in situ FTIR pattern of the $CuCO_x$ electrode that underwent two complete cycles (Figure 4a) is shown in Figure 4b. It was observed that the infrared transmittance peak belonging to the C−O bond at 1450−1500 cm^{-1} exhibited periodic changes, indicating changes in the concentration of the C−O groups.[26,32,47,48] During the discharge process, the transmittance of C−O gradually declined, suggesting an increment in the concentration of the C−O groups. Subsequently, after the charging process, the transmittance peak returned to its initial level, demonstrating the excellent reversibility of this change. Moreover, the intensity of the −OH groups at 3400−3500 cm^{-1} also exhibited variations, indicating the formation of −OH groups.[10,49−51] Figure 4c shows the Raman spectra of the pristine $CuCO_x$ powder and the $CuCO_x$ electrode, in which the additional peaks at 1340 and 1600 cm^{-1} are in accordance with the D-band and G-band of C, specifically from the conductive carbon found in the electrode.[38,52,53] The Raman peak at 1516 cm^{-1} corresponds to the asymmetric stretching of C═O, and the remaining peaks in the Raman spectra were blurred due to the annexing agents. Ex situ Raman spectra were further employed to perceive the variation of C═O in the oxalate group. Different states, marked by colored dots in Figure 4d, were tested, and the Raman patterns of wavenumbers from 900 to 2000 cm^{-1} are shown in Figure 4e. Notably, the intensities of all spectra are normalized. As the discharge process deepened, the intensity of the C═O bonds gradually decreased until fading after a complete discharge. However, the peak did not wholly disappear but was only masked by the higher D-band and G-band on both sides. When the potential returned, the signal of the C═O bands was perfectly restored, indicating the reversible reduction and rebound of the C═O concentration during the discharge−charge process. In situ FTIR and ex situ Raman spectra of copper oxalate electrodes elucidated that the content of C═O decreased while the C−O increased during the discharge process. When recharged to 0 V, both levels return to the initial condition.

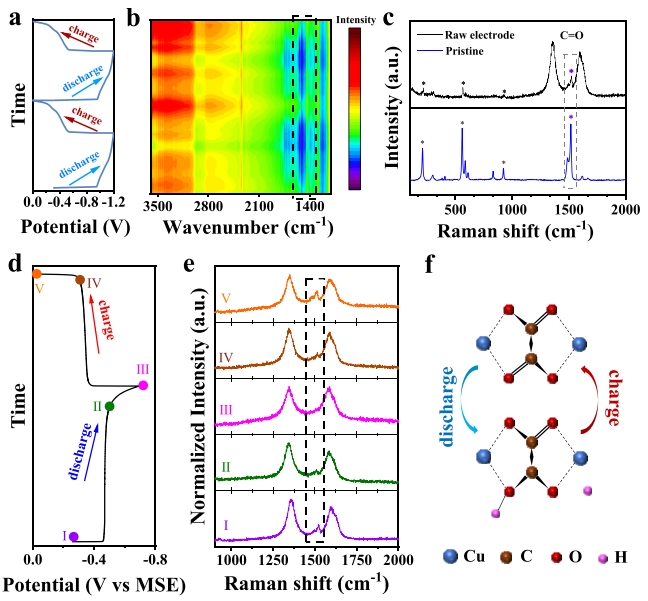

Figure 4. Redox reaction mechanism of the oxalate group. (b) In situ FTIR pattern of two full cycles as displayed in (a). (c) Comparison of Raman spectra in different states. (e) Evolution of the Raman spectra between 900 and 2000 cm^{-1} corresponding to diverse states as dotted in the charge and discharge processes in (d). (f) Schematic illustration for the proton-bonding mechanism of copper ion and the oxalate group.

The ex-situ XPS patterns of C 1s and O 1s supported a parallel conclusion. As illustrated in Figure S18c, the peak at 289.3 eV of O−C═O declined visibly after complete discharge, while the peak at 286.32 eV of C−O had a distinct uptrend. Moreover, the appearance of the peak (C−F) at 291.3 eV could be attributed to the function of the agglomerate (polyvinylidene fluoride). The identical result can also be observed in the XPS spectra of O 1s. After complete discharge, the O−C═O bond to C−O ratio significantly decreased compared with the initial state (Figure S18d).[26,54−56]

As mentioned above, the cumulative experimental data indicate the synchronous redox reactions of Cu^{2+} and $C_2O_4^{2-}$ in the $CuCO_x$ electrode. Specifically, similar to organic electrodes, the O heteroatom of C═O in the $C_2O_4^{2-}$ group serves as the oxidation centers for proton absorption/removal, thus endowing the ability of C═O to convert to C−OH by coordination with H^{+} reversibly.[10,57−59] The CV curves and in situ XRD pattern confirm that the redox reactions and proton embedding are completed in one step, demonstrating that the redox reactions of Cu^{2+} and $C_2O_4^{2-}$ occur simultaneously. Therefore, the synchronous redox reactions manifest in that during discharge Cu^{2+} is reduced to Cu^{+} to bind a proton, while sectional C═O groups open and bind another proton (C−OH) (Figure 4f). In this way, one CuC_2O_4 molecule can graft to two protons, thereby exhibiting exceptional capacity.

To further demonstrate the application potential of the $CuCO_x$ electrode in practice, we examined a full cell in which the CuFe-TBA worked as the cathode (Figure S19), $CuCO_x$ as the anode, and 0.1 M H_2SO_4 as the electrolyte (Figure 5a). Figure S19e demonstrates that the CuFe-TBA electrode can achieve a capacity close to 1 M H_2SO_4 in a 0.1 M H_2SO_4 electrolyte and can be stably cycled. This suggests that a lower concentration of the H_2SO_4 electrolyte will not impact the performance of the TBA electrode. The appropriate potential window of the full cell was determined through the LSV measurement (Figure S20). Given that $CuCO_x$ and CuFe-TBA

https://doi.org/10.1021/jacs.3c12710
J. Am. Chem. Soc. 2024, 146, 4762−4770

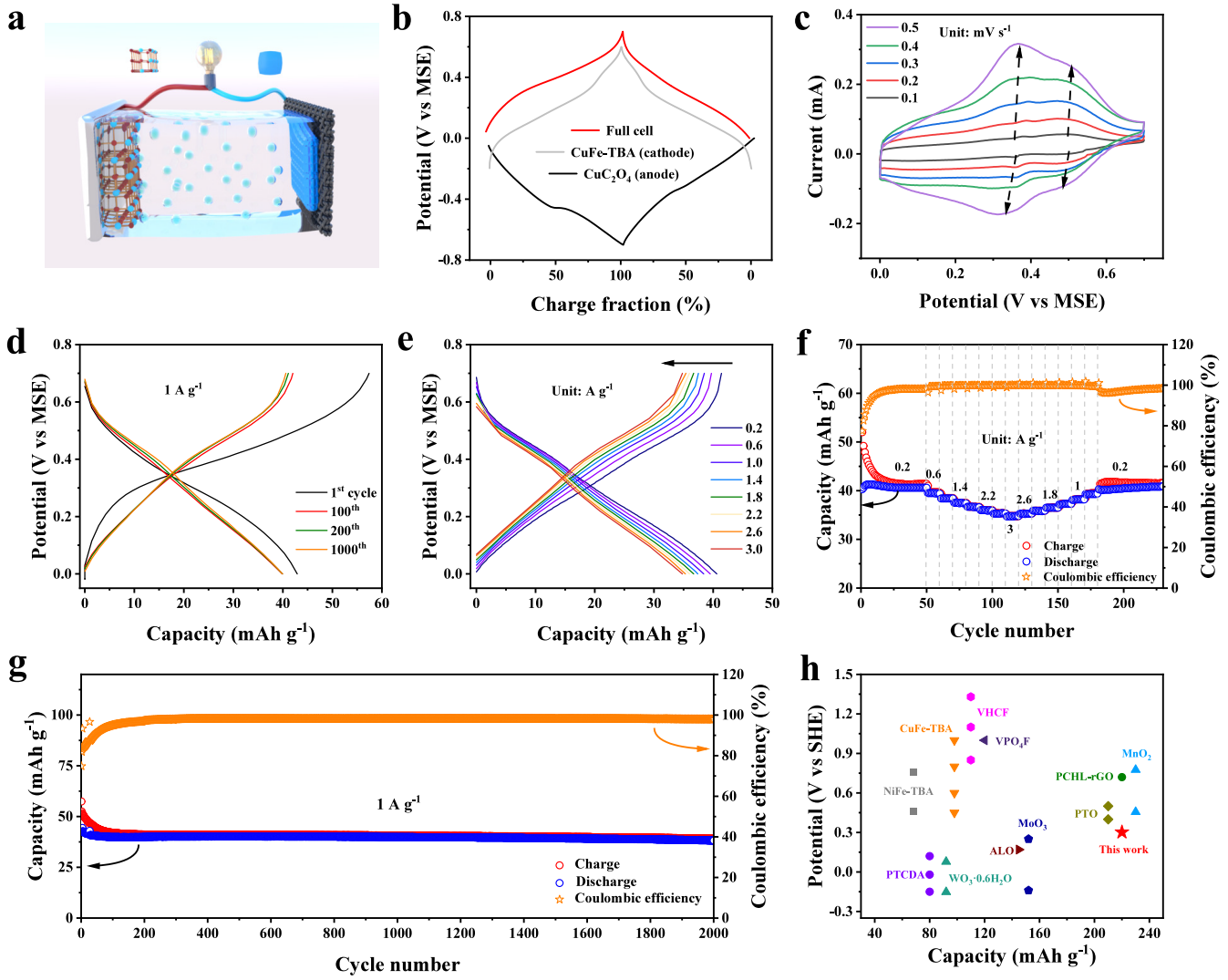

Figure 5. Electrochemical characterization of the full cell of CuFe-TBA//$CuCO_x$. (a) Schematic illustration of the full cell. (b) Feasibility of a potential window for a full cell. (c) CV curves at various scan rates. (d) GCD voltage profiles of different cycles at 1 A g^{-1}. (e) GCD profiles and (f) rate capability ranging from 0.2 to 3 A g^{-1}. (g) Cycling performance at 1 A g^{-1}. (h) Comparison of the capacity and average potential of the $CuCO_x$ electrode with the most recent reported proton electrodes.

operate within the −0.7 to 0 and −0.2 to 0.6 V ranges, respectively, the potential window of 0 to 0.7 V was selected for the full cell (Figure 5b). Figure 5c shows two pairs of distinct redox peaks in the CV curves, and the GCD curves in Figure 5d also verify a similar result. Owing to irreversible structural rearrangement and distortion, the capacity of the full battery stabilizes at 40 mAh g^{-1} (calculated according to the mass of the cathode) after 100 cycles. The well rate performance is confirmed in Figure 5e,f. The full battery exhibits a specific capacity of 42 mAh g^{-1} at the current density of 0.2 A g^{-1} and maintains 35 mAh g^{-1} at 3 A g^{-1}. Furthermore, the full battery of CuFe-TBA//$CuCO_x$ displays excellent cycling stability with a capacity retention of 95% after 2000 cycles (Figure 5g), indicating the admirable compatibility of the $CuCO_x$ anode for proton storage. Finally, as depicted in Figure 5h, $CuCO_x$ has a significant advantage as an anode for proton storage compared to the maximum capacity and average potential of commonly used electrode materials.

CONCLUSIONS

In summary, we proposed $CuCO_x$, a low-cost layered polyanionic material as a potential anode in proton batteries for the first time. The layered structure of $CuCO_x$ delivers a highly reversible ability for proton insertion/extraction. The high capacity of the $CuCO_x$ electrode is attributed to the synchronous redox behaviors of the copper ion and the oxalate group. Benefiting from the C═O group of oxalates, the $CuCO_x$ electrode can achieve double protons embedding behavior by local conversion to C−O and proton connection while Cu^{2+} undergoes a redox reaction to Cu^{+}. Furthermore, the polyanionic structure of oxalate firmly anchors oxygen atoms using covalent bonds, preventing overoxidation/over-reduction in the transition process and ensuring structural stability. Thus, the $CuCO_x$ anode displayed a remarkable specific capacity of 226 mAh g^{-1} and cycling stability (approximately 98% after 1000 cycles) at 1 A g^{-1}, surpassing those of most reported anode materials for proton batteries. This work introduces a novel avenue for developing dual-redox electrode materials for high-capacity and stable proton storage.

https://doi.org/10.1021/jacs.3c12710
J. Am. Chem. Soc. 2024, 146, 4762−4770

■ ASSOCIATED CONTENT

Supporting Information

The Supporting Information is available free of charge at https://pubs.acs.org/doi/10.1021/jacs.3c12710.

Detailed materials, experimental procedures, characterization methods, supporting figures including characterizations of copper oxalate, and ex situ XPS spectra of copper oxalate (PDF)

■ AUTHOR INFORMATION

Corresponding Authors

Lin Xu − *State Key Laboratory of Advanced Technology for Materials Synthesis and Processing, School of Materials Science and Engineering, Wuhan University of Technology, Wuhan 430070, China; Hubei Longzhong Laboratory, Wuhan University of Technology (Xiangyang Demonstration Zone), Xiangyang 441000, China; Hainan Institute, Wuhan University of Technology, Sanya 572000, China;* orcid.org/0000-0003-2347-288X; Email: linxu@whut.edu.cn

Liqiang Mai − *State Key Laboratory of Advanced Technology for Materials Synthesis and Processing, School of Materials Science and Engineering, Wuhan University of Technology, Wuhan 430070, China; Hubei Longzhong Laboratory, Wuhan University of Technology (Xiangyang Demonstration Zone), Xiangyang 441000, China; Hainan Institute, Wuhan University of Technology, Sanya 572000, China;* Email: mlq518@whut.edu.cn

Authors

Wanxin Song − *State Key Laboratory of Advanced Technology for Materials Synthesis and Processing, School of Materials Science and Engineering, Wuhan University of Technology, Wuhan 430070, China*

Jianyong Zhang − *State Key Laboratory of Advanced Technology for Materials Synthesis and Processing, School of Materials Science and Engineering, Wuhan University of Technology, Wuhan 430070, China*

Cheng Wen − *State Key Laboratory of Advanced Technology for Materials Synthesis and Processing, School of Materials Science and Engineering, Wuhan University of Technology, Wuhan 430070, China*

Haiyan Lu − *State Key Laboratory of Advanced Technology for Materials Synthesis and Processing, School of Materials Science and Engineering, Wuhan University of Technology, Wuhan 430070, China*

Chunhua Han − *State Key Laboratory of Advanced Technology for Materials Synthesis and Processing, School of Materials Science and Engineering, Wuhan University of Technology, Wuhan 430070, China*

Complete contact information is available at: https://pubs.acs.org/10.1021/jacs.3c12710

Author Contributions

All authors have given approval to the final version of the manuscript.

Notes

The authors declare no competing financial interest.

■ ACKNOWLEDGMENTS

This work was supported by the National Natural Science Foundation of China (52272234, 52172233), the National Key Research and Development Program of China (2020YFA0715000), the Key Research and Development Program of Hubei Province (2021BAA070), and the Independent Innovation Project of Hubei Longzhong Laboratory (2022ZZ-20).

■ REFERENCES

(1) Ju, Z.; Zhao, Q.; Chao, D.; Hou, Y.; Pan, H.; Sun, W.; Yuan, Z.; Li, H.; Ma, T.; Su, D.; Jia, B. Energetic Aqueous Batteries. *Adv. Energy Mater.* **2022**, *12* (27), No. 2201074.

(2) Liang, Y.; Yao, Y. Designing modern aqueous batteries. *Nat. Rev. Mater.* **2023**, *8* (2), 109−122.

(3) Jiang, J.; Liu, J. Iron anode-based aqueous electrochemical energy storage devices: Recent advances and future perspectives. *Interdiscip. Mater.* **2022**, *1* (1), 116−139.

(4) Yang, J.; Zhao, R.; Wang, Y.; Bai, Y.; Wu, C. Regulating Uniform Zn Deposition via Hybrid Artificial Layer for Stable Aqueous Zn-Ion Batteries. *Energy Mater. Adv.* **2022**, *2022*, No. 9809626.

(5) Wang, F.; Suo, L.; Liang, Y.; Yang, C.; Han, F.; Gao, T.; Sun, W.; Wang, C. Spinel $LiNi_{0.5}Mn_{1.5}O_4$ Cathode for High-Energy Aqueous Lithium-Ion Batteries. *Adv. Energy Mater.* **2016**, *7* (8), No. 1600922.

(6) Wang, M.; Meng, Y.; Li, K.; Ahmad, T.; Chen, N.; Xu, Y.; Sun, J.; Chuai, M.; Zheng, X.; Yuan, Y.; Shen, C.; Zhang, Z.; Chen, W. Toward dendrite-free and anti-corrosion Zn anodes by regulating a bismuth-based energizer. *eScience* **2022**, *2* (5), 509−517.

(7) Dai, Y.; Zhang, C.; Zhang, W.; Cui, L.; Ye, C.; Hong, X.; Li, J.; Chen, R.; Zong, W.; Gao, X.; Zhu, J.; Jiang, P.; An, Q.; Brett, D. J. L.; Parkin, I. P.; He, G.; Mai, L. Reversible Zn Metal Anodes Enabled by Trace Amounts of Underpotential Deposition Initiators. *Angew. Chem., Int. Ed. Engl.* **2023**, *62* (18), No. e202301192.

(8) Zhang, Q.; Lu, Y.; Guo, W.; Shao, Y.; Liu, L.; Lu, J.; Rong, X.; Han, X.; Li, H.; Chen, L.; Hu, Y.-S. Hunting Sodium Dendrites in NASICON-Based Solid-State Electrolytes. *Energy Mater. Adv.* **2021**, *2021*, No. 9870879.

(9) Li, J.; Yan, H.; Xu, C.; Liu, Y.; Zhang, X.; Xia, M.; Zhang, L.; Shu, J. Insights into host materials for aqueous proton batteries: structure, mechanism and prospect. *Nano Energy* **2021**, *89*, No. 106400.

(10) Shi, M.; Das, P.; Wu, Z.-S.; Liu, T.-G.; Zhang, X. Aqueous Organic Batteries Using the Proton as a Charge Carrier. *Adv. Mater.* **2023**, *35* (42), No. 2302199.

(11) Guo, H.; Wan, L.; Tang, J.; Wu, S.; Su, Z.; Sharma, N.; Fang, Y.; Liu, Z.; Zhao, C. Stable colloid-in-acid electrolytes for long life proton batteries. *Nano Energy* **2022**, *102*, No. 107642.

(12) Strietzel, C.; Sterby, M.; Huang, H.; Stromme, M.; Emanuelsson, R.; Sjodin, M. An Aqueous Conducting Redox-Polymer-Based Proton Battery that Can Withstand Rapid Constant-Voltage Charging and Sub-Zero Temperatures. *Angew. Chem., Int. Ed. Engl.* **2020**, *59* (24), 9631−9638.

(13) Xu, T.; Wang, D.; Li, Z.; Chen, Z.; Zhang, J.; Hu, T.; Zhang, X.; Shen, L. Electrochemical Proton Storage: From Fundamental Understanding to Materials to Devices. *Nano-Micro Lett.* **2022**, *14* (1), 126.

(14) Su, Z.; Chen, J.; Stansby, J.; Jia, C.; Zhao, T.; Tang, J.; Fang, Y.; Rawal, A.; Ho, J.; Zhao, C. Hydrogen-Bond Disrupting Electrolytes for Fast and Stable Proton Batteries. *Small* **2022**, *18* (22), No. 2201449.

(15) Zhou, L.; Liu, L.; Hao, Z.; Yan, Z.; Yu, X.-F.; Chu, P. K.; Zhang, K.; Chen, J. Opportunities and challenges for aqueous metal-proton batteries. *Matter* **2021**, *4* (4), 1252−1273.

(16) Wang, X.; Xie, Y.; Tang, K.; Wang, C.; Yan, C. Redox Chemistry of Molybdenum Trioxide for Ultrafast Hydrogen-Ion Storage. *Angew. Chem., Int. Ed. Engl.* **2018**, *57* (36), 11569−11573.

(17) Su, Z.; Ren, W.; Guo, H.; Peng, X.; Chen, X.; Zhao, C. Ultrahigh Areal Capacity Hydrogen-Ion Batteries with MoO_3 Loading Over 90 mg cm^{-2}. *Adv. Funct. Mater.* **2020**, *30* (46), No. 2005477.

(18) Donald, W. A.; Leib, R. D.; Demireva, M.; O'Brien, J. T.; Prell, J. S.; Williams, E. R. Directly Relating Reduction Energies of Gaseous

$Eu(H_2O)n_{3+}$, n = 55−140, to Aqueous Solution: The Absolute SHE Potential and Real Proton Solvation Energy. *J. Am. Chem. Soc.* **2009**, *131*, 13328−13337.
(19) Su, Z.; Guo, H.; Zhao, C. Rational Design of Electrode-Electrolyte Interphase and Electrolytes for Rechargeable Proton Batteries. *Nano-Micro Lett.* **2023**, *15* (1), 96.
(20) Xu, T.; Xu, Z.; Yao, T.; Zhang, M.; Chen, D.; Zhang, X.; Shen, L. Discovery of fast and stable proton storage in bulk hexagonal molybdenum oxide. *Nat. Commun.* **2023**, *14* (1), 8360.
(21) Geng, C.; Sun, T.; Wang, Z.; Wu, J. M.; Gu, Y.; Kobayashi, H.; Yang, P.; Hai, J.; Wen, W. Surface-Induced Desolvation of Hydronium Ion Enables Anatase TiO_2 as an Efficient Anode for Proton Batteries. *Nano Lett.* **2021**, *21* (16), 7021−7029.
(22) Wu, X.; Hong, J. J.; Shin, W.; Ma, L.; Liu, T.; Bi, X.; Yuan, Y.; Qi, Y.; Surta, T. W.; Huang, W.; Neuefeind, J.; Wu, T.; Greaney, P. A.; Lu, J.; Ji, X. Diffusion-free Grotthuss topochemistry for high-rate and long-life proton batteries. *Nat. Energy* **2019**, *4* (2), 123−130.
(23) Liao, M.; Cao, Y.; Li, Z.; Xu, J.; Qi, Y.; Xie, Y.; Peng, Y.; Wang, Y.; Wang, F.; Xia, Y. VPO_4F Fluorophosphates Polyanion Cathodes for High-Voltage Proton Storage. *Angew. Chem., Int. Ed. Engl.* **2022**, *61* (32), No. e202206635.
(24) Jiang, H.; Hong, J. J.; Wu, X.; Surta, T. W.; Qi, Y.; Dong, S.; Li, Z.; Leonard, D. P.; Holoubek, J. J.; Wong, J. C.; Razink, J. J.; Zhang, X.; Ji, X. Insights on the Proton Insertion Mechanism in the Electrode of Hexagonal Tungsten Oxide Hydrate. *J. Am. Chem. Soc.* **2018**, *140* (37), 11556−11559.
(25) Romann, J.; Chevallier, V.; Merlen, A.; Valmalette, J. Self-Organized Assembly of Copper Oxalate Nanocrystals. *J. Phys. Chem. C* **2009**, *113*, 5068−5074.
(26) Wu, G.; Xiao, J.; Yılmaz, M.; Zhang, T.; Yuan, S. Fusiform CuC2O4 loaded porous biochar derived from phosphoric acid-activated bagasse for gaseous ammonia capture. *J. Environ. Chem. Eng.* **2023**, *11* (2), No. 109466.
(27) Zhang, Y.-N.; Xue, L.-Y.; Zhang, Y.; Su, J.; Long, Y.-F.; Lü, X.-Y.; Wen, Y.-X. Synthesis and electrochemical performance of mesoporous MnC_2O_4 nanorod/rGO composite anode for lithium-ion batteries. *J. Mater. Sci: Mater. Electron.* **2021**, *32* (11), 15069−15079.
(28) Zhou, C.; Zhao, A.; Cheng, J.; Hou, K.; Pi, P.; Wen, X.; Xu, S. CuC_2O_4 nanoribbons on copper mesh with underwater super-oleophobicity for oil/water separation. *Mater. Lett.* **2016**, *185*, 403−406.
(29) Christensen, A. N.; Lebech, B.; Andersen, N. H.; Grivel, J.-C. The crystal structure of paramagnetic copper(II) oxalate (CuC_2O_4): formation and thermal decomposition of randomly stacked anisotropic nano-sized crystallites. *Dalton Trans.* **2014**, *43* (44), 16754.
(30) Sun, F.; Chen, T.; Li, Q.; Pang, H. Hierarchical nickel oxalate superstructure assembled from 1D nanorods for aqueous Nickel-Zinc battery. *J. Colloid Interface Sci.* **2022**, *627*, 483−491.
(31) Zhang, Y.; Wang, C.; Dong, Y.; Wei, R.; Zhang, J. Understanding the High-Performance Anode Material of $CoC_2O_4 \cdot 2H_2O$ Microrods Wrapped by Reduced Graphene Oxide for Lithium-Ion and Sodium-Ion Batteries. *Chem. - Eur. J.* **2021**, *27* (3), 993−1001.
(32) Zhang, Y.; Li, S.; Kuai, H.; Long, Y.; Lv, X.; Su, J.; Wen, Y. Proton solvent-controllable synthesis of manganese oxalate anode material for lithium-ion batteries. *RSC Adv.* **2021**, *11* (38), 23259−23269.
(33) Chen, S.; Ying, Y.; Ma, L.; Zhu, D.; Huang, H.; Song, L.; Zhi, C. An asymmetric electrolyte to simultaneously meet contradictory requirements of anode and cathode. *Nat. Commun.* **2023**, *14* (1), 2925.
(34) Li, S.; Lee, J.-H.; Hwang, S. M.; Yoo, J.-B.; Kim, H.; Kim, Y.-J. Natural Activation of CuO to $CuCl_2$ as a Cathode Material for Dual-Ion Lithium Metal Batteries. *Energy Storage Mater.* **2021**, *41*, 466−474.
(35) Wu, S.; Zhang, Z.; Lan, M.; Yang, S.; Cheng, J.; Cai, J.; Shen, J.; Zhu, Y.; Zhang, K.; Zhang, W. Lithiophilic Cu-CuO-Ni Hybrid Structure: Advanced Current Collectors Toward Stable Lithium Metal Anodes. *Adv. Mater.* **2018**, *30* (9), No. 1705830.
(36) Yin, D.; Huang, G.; Na, Z.; Wang, X.; Li, Q.; Wang, L. CuO Nanorod Arrays Formed Directly on Cu Foil from MOFs as Superior Binder-Free Anode Material for Lithium-Ion Batteries. *ACS Energy Lett.* **2017**, *2* (7), 1564−1570.
(37) Naatz, H.; Lin, S.; Li, R.; Jiang, W.; Ji, Z.; Chang, C. H.; Koser, J.; Thoming, J.; Xia, T.; Nel, A. E.; Madler, L.; Pokhrel, S. Safe-by-Design CuO Nanoparticles via Fe-Doping, Cu-O Bond Length Variation, and Biological Assessment in Cells and Zebrafish Embryos. *ACS Nano* **2017**, *11* (1), 501−515.
(38) Yao, W.; Armstrong, A. R.; Zhou, X.; Sougrati, M.-T.; Kidkhunthod, P.; Tunmee, S.; Sun, C.; Sattayaporn, S.; Lightfoot, P.; Ji, B.; Jiang, C.; Wu, N.; Tang, Y.; Cheng, H.-M. An oxalate cathode for lithium ion batteries with combined cationic and polyanionic redox. *Nat. Commun.* **2019**, *10* (1), 3483.
(39) An, S.; Hu, L.; Li, X.; Zhao, S.; Shi, M.; Yan, C. A solid-diffusion-free hydronium-ion battery with ultra-long cycle life over 8000 cycles. *Energy Storage Mater.* **2024**, *64*, No. 103076.
(40) Augustyn, V.; Come, J.; Lowe, M.; Kim, J.; Taberna, P.; Tolbert, S.; Abruna, H.; Simon, P.; Dunn, B. High-rate electrochemical energy storage through Li^+ intercalation pseudocapacitance. *Nat. Mater.* **2013**, *12* (6), 518−22.
(41) Shi, M.; Wang, R.; Li, L.; Chen, N.; Xiao, P.; Yan, C.; Yan, X. Redox-Active Polymer Integrated with MXene for Ultra-Stable and Fast Aqueous Proton Storage. *Adv. Funct. Mater.* **2022**, *33* (1), No. 2209777.
(42) Yan, M.; He, P.; Chen, Y.; Wang, S.; Wei, Q.; Zhao, K.; Xu, X.; An, Q.; Shuang, Y.; Shao, Y.; Mueller, K. T.; Mai, L.; Liu, J.; Yang, J. Water-Lubricated Intercalation in $V_2O_5 \cdot nH_2O$ for High-Capacity and High-Rate Aqueous Rechargeable Zinc Batteries. *Adv. Mater.* **2018**, *30* (1), No. 1703725.
(43) Zhao, C.; Wang, Q.; Yao, Z.; Wang, J.; Sánchez-Lengeling, B.; Ding, F.; Qi, X.; Lu, Y.; Bai, X.; Li, B.; Li, H.; Aspuru-Guzik, A.; Huang, X.; Delmas, C.; Wagemaker, M.; Chen, L.; Hu, Y. Rational design of layered oxide materials for sodium-ion batteries. *Science* **2020**, *370*, 708−711.
(44) He, W.; Xie, Q.-S.; Lin, J.; Qu, B.-H.; Wang, L.-S.; Peng, D.-L. Mechanisms and applications of layer/spinel phase transition in Li- and Mn-rich cathodes for lithium-ion batteries. *Rare Met.* **2022**, *41* (5), 1456−1476.
(45) Yin, C.; Wei, Z.; Zhang, M.; Qiu, B.; Zhou, Y.; Xiao, Y.; Zhou, D.; Yun, L.; Li, C.; Gu, Q.; Wen, W.; Li, X.; Wen, X.; Shi, Z.; He, L.; Shirley Meng, Y.; Liu, Z. Structural insights into composition design of Li-rich layered cathode materials for high-energy rechargeable battery. *Mater. Today* **2021**, *51*, 15−26.
(46) Hesabizadeh, T.; Jebari, N.; Madouri, A.; Hallais, G.; Clark, T.; Behura, S.; Herth, E.; Guisbiers, G. Electric-Field-Induced Phase Change in Copper Oxide Nanostructures. *ACS Omega* **2021**, *6* (48), 33130−33140.
(47) Chen, D.; Zhou, Z.; Feng, C.; Lv, W.; Wei, Z.; Zhang, K. H. L.; Lin, B.; Wu, S.; Lei, T.; Guo, X.; Zhu, G.; Jian, X.; Xiong, J.; Traversa, E.; Dou, S. X.; He, W. An Upgraded Lithium Ion Battery Based on a Polymeric Separator Incorporated with Anode Active Materials. *Adv. Energy Mater.* **2019**, *9* (15), No. 1803627.
(48) Yan, X.; Wang, F.; Su, X.; Ren, J.; Qi, M.; Bao, P.; Chen, W.; Peng, C.; Chen, L. A Redox-Active Covalent Organic Framework with Highly Accessible Aniline-Fused Quinonoid Units Affords Efficient Proton Charge Storage. *Adv. Mater.* **2023**, *35* (44), No. 2305037.
(49) Yang, X.; Ni, Y.; Lu, Y.; Zhang, Q.; Hou, J.; Yang, G.; Liu, X.; Xie, W.; Yan, Z.; Zhao, Q.; Chen, J. Designing Quinone-Based Anodes with Rapid Kinetics for Rechargeable Proton Batteries. *Angew. Chem., Int. Ed. Engl.* **2022**, *61* (39), No. e202209642.
(50) Nguyen, T. P.; Easley, A. D.; Kang, N.; Khan, S.; Lim, S. M.; Rezenom, Y. H.; Wang, S.; Tran, D. K.; Fan, J.; Letteri, R. A.; He, X.; Su, L.; Yu, C. H.; Lutkenhaus, J. L.; Wooley, K. L. Polypeptide organic radical batteries. *Nature* **2021**, *593* (7857), 61−66.
(51) Dong, X.; Li, Z.; Luo, D.; Huang, K.; Dou, H.; Zhang, X. Pre-Protonated Vanadium Hexacyanoferrate for High Energy-Power and

Anti-Freezing Proton Batteries. *Adv. Funct. Mater.* **2023**, *33* (11), No. 2210473.
(52) Huang, L.; Shen, S.; Zhong, Y.; Zhang, Y.; Zhang, L.; Wang, X.; Xia, X.; Tong, X.; Zhou, J.; Tu, J. Multifunctional Hyphae Carbon Powering Lithium-Sulfur Batteries. *Adv. Mater.* **2022**, *34* (6), No. 2107415.
(53) Li, J.; Zhang, K.; Zhao, Y.; Wang, C.; Wang, L.; Wang, L.; Liao, M.; Ye, L.; Zhang, Y.; Gao, Y.; Wang, B.; Peng, H. High-Efficiency and Stable Li-CO_2 Battery Enabled by Carbon Nanotube/Carbon Nitride Heterostructured Photocathode. *Angew. Chem., Int. Ed. Engl.* **2022**, *61* (4), No. e202114612.
(54) Nakhanivej, P.; Yu, X.; Park, S. K.; Kim, S.; Hong, J. Y.; Kim, H. J.; Lee, W.; Hwang, J. Y.; Yang, J. E.; Wolverton, C.; Kong, J.; Chhowalla, M.; Park, H. S. Revealing molecular-level surface redox sites of controllably oxidized black phosphorus nanosheets. *Nat. Mater.* **2019**, *18* (2), 156−162.
(55) Ye, C.; Wang, G.; Yuan, H.; Li, J.; Ni, K.; Pan, F.; Guo, M.; Wu, Y.; Ji, H.; Zhang, F.; Qu, B.; Tang, Z.; Zhu, Y. Microfluidic Oxidation of Graphite in Two Minutes with Capability of Real-Time Monitoring. *Adv. Mater.* **2022**, *34* (15), No. 2107083.
(56) Zhang, J.; Ren, M.; Wang, L.; Li, Y.; Yakobson, B. I.; Tour, J. M. Oxidized Laser-Induced Graphene for Efficient Oxygen Electrocatalysis. *Adv. Mater.* **2018**, *30* (21), No. 1707319.
(57) Emanuelsson, R.; Sterby, M.; Strømme, M.; Sjödin, M. An All-Organic Proton Battery. *J. Am. Chem. Soc.* **2017**, *139* (13), 4828−4834.
(58) Kim, D. J.; Yoo, D.-J.; Otley, M. T.; Prokofjevs, A.; Pezzato, C.; Owczarek, M.; Lee, S. J.; Choi, J. W.; Stoddart, J. F. Rechargeable aluminium organic batteries. *Nat. Energy* **2019**, *4* (1), 51−59.
(59) Zhu, M.; Zhao, L.; Ran, Q.; Zhang, Y.; Peng, R.; Lu, G.; Jia, X.; Chao, D.; Wang, C. Bioinspired Catechol-Grafting PEDOT Cathode for an All-Polymer Aqueous Proton Battery with High Voltage and Outstanding Rate Capacity. *Adv. Sci. (Weinh)* **2022**, *9* (4), No. 2103896.

https://doi.org/10.1021/jacs.3c12710
J. Am. Chem. Soc. 2024, 146, 4762−4770